SPECIAL ISSUE ARTICLE

PROGRESS IN PHOTOVOLTAICS WILEY

Wafer-bonded two-terminal III-V//Si triple-junction solar cell with power conversion efficiency of 36.1% at AM1.5g

Patrick Schygulla[1] | **Ralph Müller**[1] | **Oliver Höhn**[1] | **Michael Schachtner**[1] |
David Chojniak[1] | **Andrea Cordaro**[2] | **Stefan Tabernig**[2] | **Benedikt Bläsi**[1] |
Albert Polman[2] | **Gerald Siefer**[1] | **David Lackner**[1] | **Frank Dimroth**[1]

[1]Fraunhofer Institute for Solar Energy Systems ISE, Freiburg, Germany

[2]NWO-Institute AMOLF, Amsterdam, The Netherlands

Correspondence
Patrick Schygulla, Fraunhofer Institute for Solar Energy Systems ISE, Freiburg, Germany.
Email: patrick.schygulla@ise.fraunhofer.de

Abstract

In this work, we present the fabrication and analysis of a wafer-bonded GaInP/GaInAsP//Si triple-junction solar cell with 36.1% conversion efficiency under AM1.5g spectral illumination. The new cell design presents an improvement over previous III-V//Si triple-junction cells by the implementation of a rear-heterojunction for the middle cell. Furthermore, an advanced metallodielectric rear-side grating was used for light trapping enhancement in the silicon bottom cell that increased the silicon subcell current by 1.4 mA/cm^2. The external radiative efficiency was quantified to be 1.5 times higher compared to a reference device with a GaInAsP homojunction middle cell. A luminescent coupling factor of 0.46 between the middle and bottom subcell was determined. The share of recombination in the space-charge region was experimentally shown to be insignificant as intended by the rear-heterojunction design. Overall, the open-circuit voltage of the middle cell increased by 61 mV compared to the previous generation. Given the established long-term stability of III-V and silicon-based solar cells, these results are promising steps towards the future employment of III-V/Si tandem solar cells.

KEYWORDS

back-side reflector, external radiative efficiency, GaInAsP, III-V//Si multi-junction solar cells, luminescence coupling, MOVPE, rear-heterojunction, silicon-based tandem solar cells

1 | INTRODUCTION

The record efficiency of silicon single-junction solar cells is close to its theoretical efficiency limit of 29.4%–29.5%.[1,2] Further increasing the cell efficiency[3] is an important driver for photovoltaics system cost reduction. Hence, there is the strong need for new solar cell concepts exceeding the silicon single-junction efficiency limit. Multi-junction solar cells are a promising concept to this end with demonstrated efficiencies of up to 39.5% for a triple-junction cell fully made from III-V semiconductors.[4] Such cells are grown by epitaxial deposition on an expensive GaAs or InP substrate. Hence, we investigated the efficiency potential of III-V top structures combined with a silicon bottom cell to improve the efficiency-to-cost ratio.

Wafer-bonded III-V//Si multi-junction solar cells were the first monolithic silicon-based tandem cells to surpass a conversion efficiency of 30%. In the past, we have shown further efficiency improvements by (a) the inclusion of a TOPCon surface passivation of the silicon bottom cell together with the integration of a diffractive light scattering structure on the rear side, reaching 33.3%,[5] (b) the employment of an absorber material with a higher band gap in the second

junction, AlGaAs instead of GaAs, reaching 34.1%,[6] and (c) the employment of a material with higher minority carrier lifetimes, GaInAsP instead of AlGaAs, reaching 35.9%.[7]

An alternative approach to a monolithic connection consists in mechanically stacking the III-V structure on top of the silicon bottom structure in a four-terminal design. This releases the constraint of current matching between the subcells and lattice constant matching between the crystals, which enhances the availability space of suitable absorber materials. The electrical power produced in the subcells is extracted separately. In theory, the efficiency limit of the four-terminal design is slightly higher than of the two-terminal design. In practice, however, parasitic absorption and reflection in the gap between the cells as well as the more complex electrical interconnection of neighbouring cells are major disadvantages. The highest efficiency achieved with this approach amounts to 35.9% at AM1.5g with a $Ga_{0.51}In_{0.49}P$/GaAs + Si layer stack.[8]

Other promising tandem cell concepts involving silicon bottom cells are dual-junctions employing a perovskite top cell. With this technology, the highest efficiency to date amounts to 33.9% on a $1 cm^2$ device. Solar cells including perovskite absorbers exhibit degradation over time, for which an ultimate solution has not yet been found, though.[9] Combining more than two junctions using perovskite absorbers is challenging due to wet-chemical processing issues and reduced availability of materials at the required higher band gaps. The highest efficiency for a monolithic triple-junction perovskite/perovskite/silicon device amounts to 20%.[10]

Here, we present a GaInP/GaInAsP//Si triple-junction solar cell with a further improved heterojunction structure of the III-V layer stack, combined with the previously demonstrated metallodielectric light trapping back-side reflector. We measured a conversion efficiency of 36.1%, the highest value observed for a Si-based solar cell. The high efficiency enables a detailed study of the carrier collection quantum efficiency and spontaneous emission processes that determine the high efficiency. The long-term reliability of III-V//Si triple-junction solar cells has been confirmed in previous studies by damp heat and accelerated aging tests with relative degradation below 5%.[11] III-V semiconductor layers are deposited at temperatures exceeding 600°C so possible degradation processes during operation can scarcely affect the cell materials.

2 | METHODS

2.1 | Epitaxial growth

III-V semiconductor layers were epitaxially grown lattice matched to GaAs by metalorganic vapour phase epitaxy in a commercial AIX2800G4 reactor from AIXTRON. 4″ (001)-oriented GaAs wafers with an offcut of 6° into the [111]-B direction were used as substrates. TMAl, TMGa, TMIn, AsH₃, PH₃, DMZn, and SiH₄ were used as precursors. In both the middle and the top cell, a rear-heterojunction design was employed. The first reason for this choice is the higher minority carrier lifetime of n-GaInAsP, the only absorber material in

the rear-heterojunction, compared to p-GaInAsP,[12] the thickest part of the absorber in a homojunction. The second reason is the reduction of the dark current in the space charge region because of the increased band gap inside the space charge region at the rear-side of the absorber.[13] The middle rear-heterojunction solar cell consists of a 1800 nm thick $n-Ga_{0.91}In_{0.09}As_{0.83}P_{0.17}$:Zn absorber, a 25 nm thick $n-Al_{0.52}In_{0.48}P$:Si front-surface field, and a 70 nm thick $p-Al_{0.6}Ga_{0.4}As$:C back-surface field which were grown with optimised growth conditions as stated in a previous publication.[12] Tunnel junctions made from p-AlGaAs/n-GaAs/n-AlGaAs were employed for the series interconnection of the solar cells.

2.2 | Solar cell processing

The middle cell was deposited first and the top cell second on the GaAs substrate to reduce the voltage drop in the top cell due to a high thermal load.[7] The upright growth fashion made it necessary to temporarily bond the epitaxial structure to a sapphire wafer as mechanical support. After that, the GaAs substrate was removed by wet chemical etching with citric acid. Then, the exposed bond layer was chemically mechanically polished by the company III/V-Reclaim. Next, a direct wafer bond to a TOPCon silicon cell was performed before the temporary bond could be released again by thermal slide at 190°C. Subsequently, the solar cells were processed using photolithography, mesa etching, metal contact formation, and sputter deposition of an anti-reflection coating (ARC). Twelve solar cells with a size of $2 \times 2 cm^2$ and a metal grid optimised for one-sun operation were processed on each wafer. After solar cell processing, the wafers were nano-imprinted with a diffractive grating on the rear side at AMOLF using substrate conformal imprint lithography. The rear-side grating is designed to enhance the optical path length in the silicon bottom cell and thus to increase the bottom subcell current. It minimises light scattering from the back-side reflector in normal direction and enhances large-angle scattering in the Si cell, while minimising parasitic absorption in the metal. More details on the solar cell processing can be found in the literature.[5,7,14] The final layer stack is shown in Figure 1.

2.3 | Characterisation

The solar cells were characterised by external quantum efficiency and current–voltage measurements before and after the diffractive rear-side grating was applied to evaluate the current gain. The *IV*-curves were recorded under calibrated spectral conditions of AM1.5g (IEC 60904-3:2019 (ed.4)) in the Fraunhofer ISE Calibration Laboratory (CalLab). Current–voltage characteristics were measured using a hard mask with an aperture area of $3.987 cm^2$, which is slightly lower than the mesa area of the solar cells, in order to prevent a lateral current contribution from the silicon bottom junction outside of the mesa area.

To analyse the impact of the rear-heterojunction middle cell, spectrally resolved electroluminescence measurements were conducted. Along with the external quantum efficiency, the external radiative
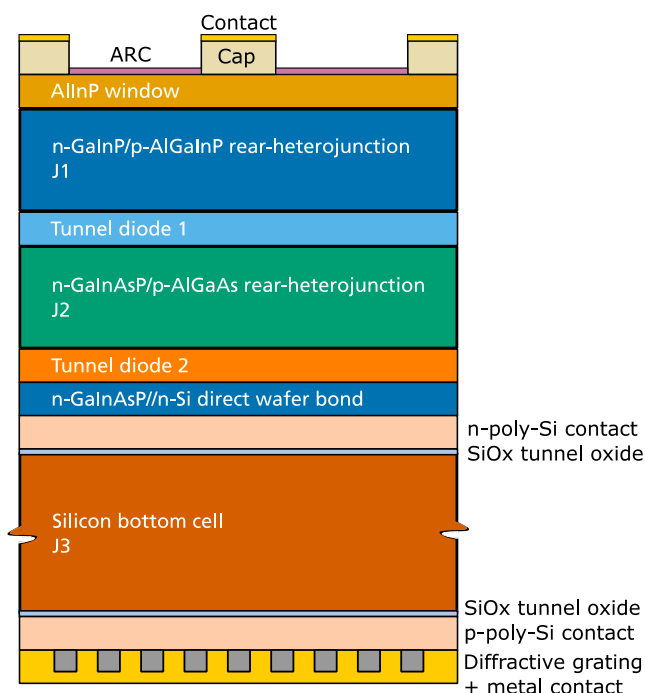
—WILEY

FIGURE 1 Layer stack of the III-V//Si triple-junction solar cell. The GaInP/GaInAsP top structure was attached to a TOPCon silicon bottom cell by surface-activated direct wafer bonding. The rear-side grating was implemented by nanoimprint lithography. [Colour figure can be viewed at wileyonlinelibrary.com]

FIGURE 2 Current–voltage characteristics of the champion GaInP/GaInAsP//Si triple-junction solar cell measured in the Fraunhofer ISE CalLab under a calibrated AM1.5g spectrum.

efficiency was determined by means of the reciprocity relations.[15] j_{sc}-V_{oc}-pairs at around 0.25 suns, 0.5 suns, and 1 sun were acquired from current–voltage characteristics in a sun simulator setup to provide an absolute calibration of the electroluminescence results for quantitative determination of the subcell voltages. As a reference, a triple-junction solar cell with a GaInAsP-homojunction middle cell from a previous batch was studied as well.

Additionally, the subcell currents were analysed under different spectral conditions to determine the luminescent coupling between subcells and the radiative recombination current of the top cells. For this advanced characterisation method, a Wavelabs SINUS 220 LED based solar simulator equipped with 20 spectrally different LED light sources was used.[16] Using the different LED channels, the injection level on each subcell was varied in a systematic manner while the remaining subcells were light biased at AM1.5g conditions. A custom software was used to control the illumination unit of the solar simulator while the spectral adjustment of the individual light sources was realised using the procedure described Chojniak et al..[17]

3 | RESULTS

3.1 | Current–voltage characteristics

The current champion solar cell has a power conversion efficiency of 36.1% under the AM1.5g spectrum as was determined by a calibrated
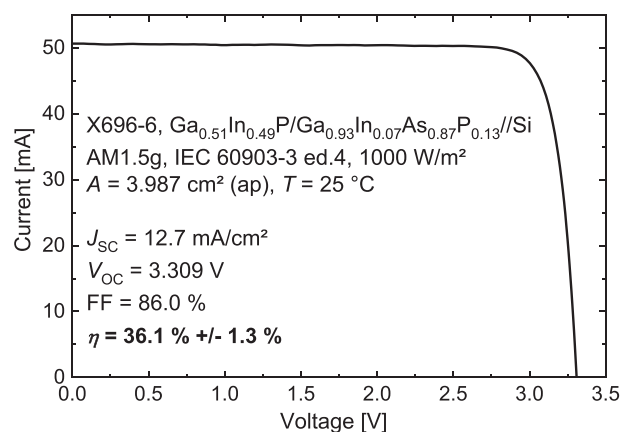
current–voltage measurement that is shown in Figure 2. The main reason for the higher efficiency compared to the last generation of III-V//Si triple-junction solar cells made at Fraunhofer ISE is the increase in open-circuit voltage by 61 mV as the comparison of the last wafer-bonded silicon-based triple-junction cell parameters in Table 1 confirms. The major difference compared to the previous generation is the inclusion of a rear-heterojunction cell configuration in place of the former homojunction cell design for the middle cell. The short-circuit current of the last generations of devices was between 12.4 and 13.1 mA/cm^2 because of slight variations in the current matching of the subcells. Cells with a lower j_{sc} which is caused by current mismatch rather than parasitic absorption, show a higher fill factor as expected, for example, X610-6 and X696-6. The fill factor of X696-6 is increased by 2% compared to X633-7 because of the current mismatch, which reduced the j_{sc} by 3%. Consequently, the gain in efficiency for our current champion solar cell can be attributed to the higher V_{oc} and not the higher fill factor. From diode-model fits, the parallel resistance was determined for each of the devices. Over the last generations it improved from around 20 kΩ cm^2 to above 35 kΩ cm^2. For such lattice-matched solar cells without threading dislocations, the main contribution to the parallel resistance stems from purity of technological processes impacting the cell edge such as residues during mesa etching rather than material-related defects. At present, the efficiency drop associated to the parallel resistance amounts to 0.21%$_{abs}$.

3.2 | External quantum efficiency

The external quantum efficiency (EQE) of the champion cell X696-6 is shown in Figure 3. The subcell current density is calculated from the injection current variation experiments explained below. That analysis shows that the middle cell is current limiting with 12.6 mA/cm^2. The sum of the subcell currents amounts to 38.9 mA/cm^2 which implies current matched conditions at a j_{sc} of around 13.0 mA/cm^2 at the

TABLE 1 Solar cell parameters of the last four generations of III-V//Si triple-junctions produced at Fraunhofer ISE. The 36.1% record cell had a back-side reflector produced at AMOLF. The quantity with the largest improvement compared to the previous generation is marked bold.

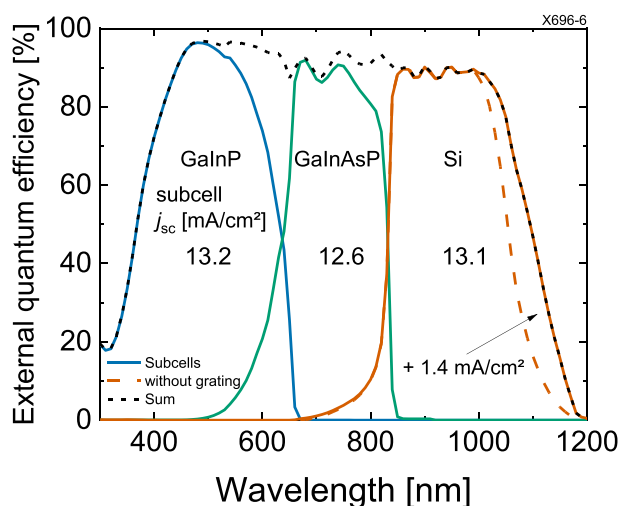| Year	Solar cell device	Middle cell	V_{oc} [V]	j_{sc} [mA/cm²]	FF [%]	Efficiency [%]
2017	XE8-11[5]	GaAs homojunction	**3.127**	**12.7**	83.8	33.3
2020	X610-6[6]	AlGaAs homojunction	**3.177**	12.4	86.4	34.1
2021	X633-7[7]	GaInAsP homojunction	**3.248**	**13.1**	84.3	35.9
2023	X696-6	GaInAsP rear-heterojunction	**3.309**	12.7	86.0	36.1

FIGURE 3 External quantum efficiency of the three subcells (solid line) and of the entire triple-junction solar cell (black, dotted line). The quantum efficiency of the silicon bottom cell before the imprint of the diffractive rear-side grating is shown by the orange dashed line. [Colour figure can be viewed at wileyonlinelibrary.com]

currently prevailing optical and electrical performance. Thus, the middle cell is limiting by 0.4 mA/cm². The difference of 0.1 mA/cm² in the short-circuit current density of the entire triple-junction, 12.7 mA/cm², compared to the subcell current density of the middle cell, 12.6 mA/cm², is caused by two effects. The first effect is luminescence coupling from the top to the middle cell. Considering the difference in subcell current between the top and middle cell, 0.6 mA/cm², this implies that around a fifth to a quarter of the excessively injected charge carriers recombine radiatively in the top cell and these photons are then reabsorbed in the middle cell. The second effect is a small decrease in current density from $V = 0$ towards the short-circuit point of the current limiting subcell, at $V = V_{oc} - V_{oc,j2}$ due to a finite parallel resistance.

Before the nanoimprint of the diffractive rear-side structure the short-circuit current density was limited by the silicon bottom cell with 11.7 mA/cm². Hence, the light path enhancement that leads to increased absorption in the long-wavelength regime close to the absorption threshold for silicon, around 1100 nm, resulted in an increase in current density by 1.4 mA/cm² to a total value of 13.1 mA/cm². Differently designed versions of a rear-side diffractive

structure in previous experiments lead to a current density gain of 1.1 mA/cm² in the silicon bottom cell.[18]

If the subcell currents of a multi-junction solar cell are perfectly matched, then the rounding of the individual *IV*-curves at the maximum power point adds up and the fill factor of the *IV*-curve of the entire device is reduced. Conversely, in strong current-mismatched conditions the fill factor is dominated by the fill factor of the current limiting subcell.[19] The device XE8-11 had a current mismatch of only 0.1 mA/cm² so its fill factor of 83.8% can be regarded as a lower boundary value for this cell design. If the available solar resource was distributed more evenly between all subcells, similar to X633-7, while maintaining the material quality and thus the open-circuit voltage, the power conversion efficiency could still be improved by 0.4%$_{abs}$ to 36.5% with mere adjustments to the absorber thicknesses.

3.3 | Subcell voltage and external radiative efficiency

The analysis of the electroluminescence signal at various injection conditions revealed the middle cell voltages at the corresponding concentration levels. From these data, a pseudo-*IV*-curve without resistive losses can be constructed similar to the suns-V_{oc} method[20] as was done in Figure 4. Fitting the two-diode model to the data[21] with the series resistance set to 0 due to the nature of the pseudo-*IV*-curve, one can obtain the dark currents j_{01} and j_{02} associated with recombination in the bulk or the space charge region, respectively. The ratio of the dark recombination currents $\varphi = \frac{j_{02}}{2\sqrt{j_{01}}}$ provides a convenient measure of the relative strength of non-radiative recombination in the space charge region compared to radiative recombination in the bulk of the cell.[22] In order to compare the same numerical order of magnitude, the square root of j_{01} is taken accounting for the different ideality factors. Since the dark recombination current decreases with increasing band gap, a ratio provides a better means of comparison between different materials rather than absolute dark current densities. Comparing the ratio of the two subcells, the intended suppression of recombination in the space charge region by the rear-heterojunction design can be quantified. We obtain $\varphi_{homo} = 0.16$ $\sqrt{A/cm^2}$ and $\varphi_{rear-hetero} = 0.04$ $\sqrt{A/cm^2}$, thus a fourfold reduction in the non-radiative depletion zone recombination. The band gaps of the two middle cells are not identical with X696-6 having a slightly higher band gap by 10 meV. Hence, the lifetime improvement in the middle cell cannot account for the entire voltage improvement of this device.
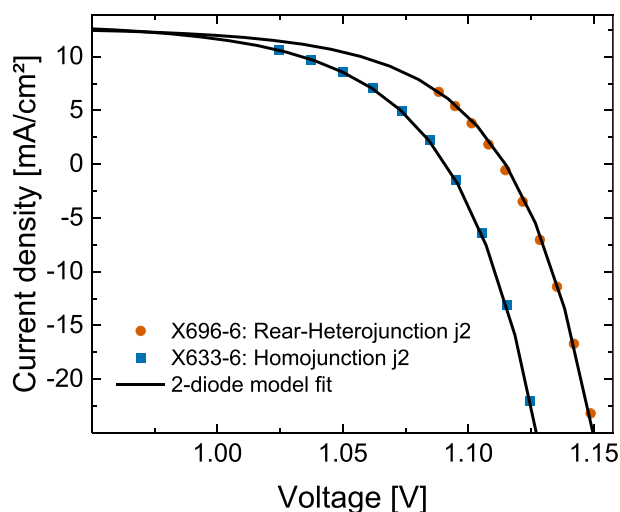
FIGURE 4 Pseudo-*IV*-curves of a rear-heterojunction (orange circles) and a homojunction middle cell (blue squares) as constructed from the subcell voltage measurements. The black solid lines show a two-diode model fit to the data. [Colour figure can be viewed at wileyonlinelibrary.com]
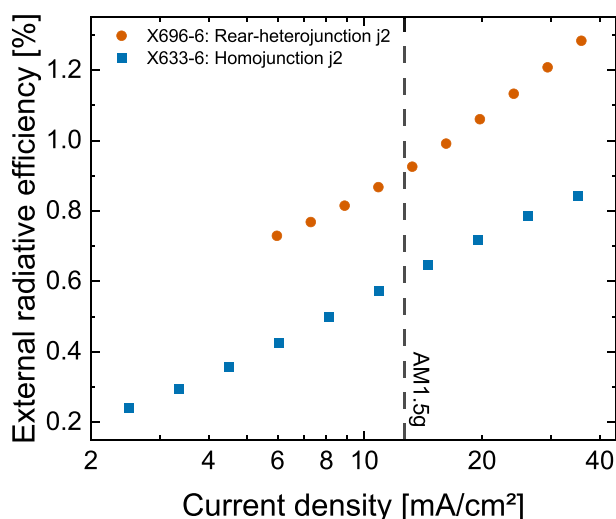

FIGURE 5 External radiative efficiency of the middle cell of a III-V//Si triple-junction solar cell in homojunction (blue, squares) and rear-heterojunction configuration (orange, circles). The current density condition that corresponds to irradiation by AM1.5g is marked by the vertical dashed line. [Colour figure can be viewed at wileyonlinelibrary.com]

Since the top and bottom cells were nominally the same the rest of the voltage gain remains unexplained.

As shown in Figure 5, the external radiative efficiency (ERE) of the middle cell with a rear-heterojunction design is significantly higher than the ERE of the one with a homojunction design. Not only the absolute value of the ERE is higher for the rear-heterojunction but also the logarithmic increase is faster. For the homojunction case there is a non-negligible contribution of dark

current $j_{02}\left(\exp\left(\frac{qV}{n_2 k_B T}\right) - 1\right)$, resulting from charge carrier recombination in the space-charge region. Since this recombination is associated with a larger ideality factor n_2 than recombination in the bulk crystal the corresponding prefactor is smaller. In a rear-heterojunction solar cell, recombination in the space-charge region is almost completely suppressed as there is scarcely any absorption taking place in the depletion zone by design.[23] Note that the absolute value of the ERE appears small in comparison to a thin-film GaAs single-junction solar cell on a mirror with 35.7% external radiative efficiency.[24] This is due to the fact that in the case of the middle subcell of a triple-junction cell with a thick silicon bottom subcell only little photon recycling inside the middle subcell can occur. Most of the radiatively emitted photons are either lost to the front side or reabsorbed in the bottom subcell. This phenomenon is discussed in the following section and manifests an intrinsic reduction of the ERE.

3.4 | Luminescence coupling

The high amount of radiative recombination in the middle cell results in luminescence coupling from the second to the third junction. Photons that are emitted after radiative recombination of charge carriers in the middle cell have a certain probability of leaving the junction towards the bottom and be reabsorbed by the bottom cell. If the bottom cell limits the overall current, then this luminescent contribution increases the short-circuit current. Following the procedure suggested by Steiner et al.,[25] the irradiance of each subcell was systematically decreased and increased with respect to AM1.5g 1-sun conditions while the other subcells were biased with light to maintain an AM1.5g injection level. The measured short-circuit currents for the different irradiance conditions are shown in Figure 6.

On the left side of the diagram where the slopes are constant, the subcell for which the photocurrent is varied is current limiting in each case. The second junction is current limiting at 1 sun. This is why the photocurrent of the second junction must be increased above 1 sun to reach current matching with the top cell at 13.2 mA/cm^2. Then, the top cell becomes limiting and the overall current stagnates. For the first junction, one can see that upon further increase of the photocurrent beyond 0.96 suns the overall current increases again due to luminescent coupling from the first to the second junction with the coupling factor η_{12}. If the irradiance of the third junction is decreased below around 0.97 suns, then that junction becomes limiting. From the curve shape of the injection variation of the bottom cell, the luminescence coupling factor η_{23} from the second to the third junction can be extracted. The second junction is optically thick for light emitted by the first junction so the contribution of coupled light from the first directly to the third junction can be neglected.

The coupling factors η_{ij} are a combination of the optical properties of the layer stack determined by the refractive indices of the subcells and all intermediate layers, and the internal radiative efficiency. Another electrical parameter $\varphi = \frac{j_{02}}{2\sqrt{j_{01}}}$ determines the strength of the coupling, in particular, for small excess currents. The higher this ratio the larger is the share of non-radiative recombination in the
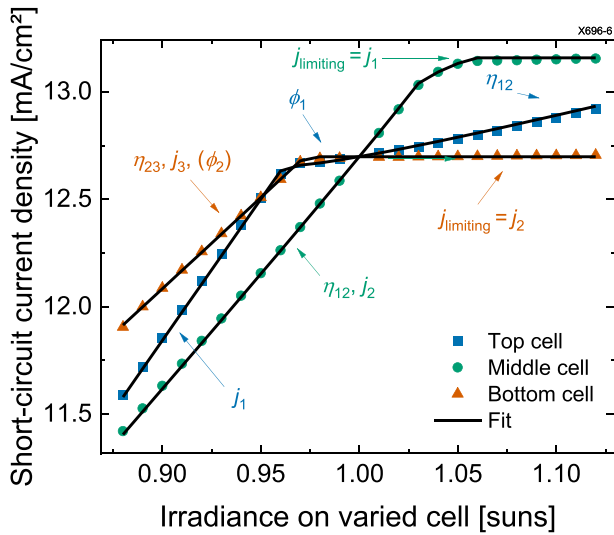
FIGURE 6 Measured short-circuit current of the III-V//Si 3j champion device upon selective variation of the photocurrent in the top (blue squares), middle (cyan circles), and bottom junction (orange triangles) around AM1.5g conditions at 1 sun. The other junctions are biased at the 1-sun conditions, respectively. The fitted curves to the data are shown by solid black lines. The arrows indicate which model parameters can be best determined in which regimes of the data. Note that these parameters indirectly influence other regimes as well. [Colour figure can be viewed at wileyonlinelibrary.com]

space-charge region with a diode ideality factor of 2 and fewer photons are emitted that could boost the current of lower lying junctions. The overall short-circuit current is determined by

$$j_{sc} = \min \begin{cases} j_1 \\ j_2 + j_{lc,12} \\ j_3 + j_{lc,23} \end{cases}$$

where j_i is the externally injected photocurrent and $j_{lc,ij}$ the light coupling from junction i to junction j. The latter contributions can be derived as an explicit equation.[25]

$$j_{lc,12} = \frac{\eta_{12}}{(1+\eta_{12})^2} \left(\sqrt{\varphi_1^2 + (1+\eta_{12})(j_1 - j_2)} - \varphi_1 \right)^2$$

and an implicit equation

$$j_{lc,23} = \eta_{23} \left(\sqrt{\varphi_2^2 + j_2 - j_3 - j_{lc,23} + \eta_{12} \left(\sqrt{\varphi_1^2 + j_1 - j_3 - j_{lc,23}} - \varphi_1 \right)^2} - \varphi_2 \right)^2 .$$

The fit parameters that can reproduce the data of Figure 6 are $\eta_{12} = 0.27 \pm 0.03$, $\eta_{23} = 0.46 \pm 0.07$, $\varphi_1 = (0.7 \pm 0.2) \sqrt{A/cm^2}$, and $\varphi_2 = (0.0 \pm 0.2) \sqrt{A/cm^2}$. Within the uncertainty, φ_2 cannot be distinguished from 0, which agrees with the rear-heterojunction design of the middle subcell that is built in a way to reduce recombination in the space charge region. The low value of φ_2 is also consistent within

the confidence interval with the ratio of dark currents of 0.04 $\sqrt{A/cm^2}$ that was obtained from the pseudo-IV-curves in the previous section. The coupling factor η_{12} confirms the short-circuit current density result from the calibrated AM1.5g IV-curve, which is higher than the subcell current of the limiting middle cell by around a quarter of the excess photocurrent in the top cell. Comparing these values to a GaInP/GaAs/GaInAs triple-junction solar cell employing three homojunctions the coupling of the top to the middle cell, $\eta_{12} = 0.240$, was reported to be very similar to our value, while the coupling from the middle to the bottom cell, $\eta_{23} = 0.888$, was higher than in our case.[22] The main reason is probably the supreme crystal quality of the GaAs solar cell exhibiting a high radiative efficiency. Another difference between the cells is the metamorphic buffer of the cell from literature, which enabled a more gradual transition of the refractive index and thus less reflection to the front side. In our case, the direct waferbond between GaInAsP and silicon, $n_{Si}(800\,nm) = 3.694$,[26] with the thin amorphous layers in between, $n_{a-Si}(800\,nm) = 3.896$,[27] manifests a more abrupt refractive index change, which results in more reflection. This is a beneficial effect since photon recycling within the subcell is energetically more advantageous than luminescence coupling. The reason is that the photon energy is better exploited in the former case.

3.5 | Optical loss analysis

To identify potential for further improvements of the presented triple-junction design, the optical losses in different parts of the solar cell structure were quantified using the transfer-matrix formalism[28] implemented in Python.[29] All epitaxial layers were first modelled with their nominal thicknesses and compositions and in a second step the layer thicknesses were adjusted to fit the absorption to the measured external quantum efficiency shown in Figure 3. Also, the composition of the GaInAsP middle cell was slightly adjusted by means of optical parameter morphing[30] to match the experimentally determined absorption edge. In Figure 7, the results of the optical loss analysis are presented. From the entire energy of the AM1.5g spectrum, 26.3% is lost due to imperfect absorption of the light. Around two thirds of this loss can be attributed to losses associated with photon escape from the silicon cell and parasitic absorption in the diffractive structure. Since the plasmonic resonances occurring in the diffractive structure are not easy to be modelled accurately, only the sum of escape and rear-side absorption in the structure is shown in Figure 7. Silicon has a higher band gap than would be ideal for a bottom cell of a triple-junction solar cell, which is why a rather large amount of infrared light is not captured by the bottom cell. The second largest contribution stems from reflection. Since the anti-reflective coating (ARC) was designed to maximise the total absorbed photocurrent in the subcells, the reflection loss mainly occurs in the far infrared range, in which light cannot be absorbed anyway in the given design, and in the ultraviolet range. Besides, front-side absorption of high-energy photons in the ARC layers, the AlInP window, and the upper tunnel diode are significant contributions whereas the lower tunnel diode and the bond
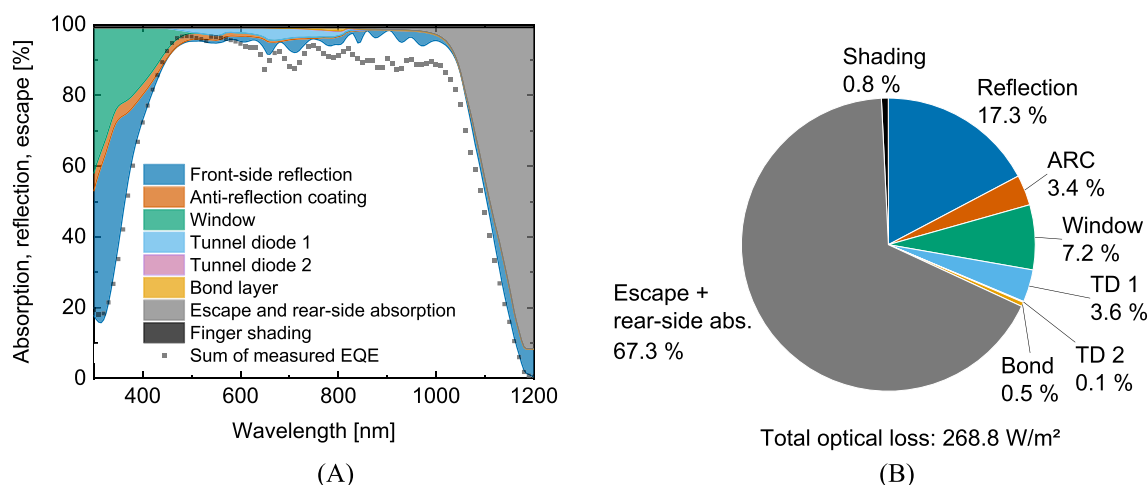
FIGURE 7 Optical loss analysis of the champion cell X696-6 including reflection, escape, and parasitic absorption losses as calculated by a transfer-matrix formalism. (A) Spectrally resolved loss channels in each part of the cell that do not contribute to the subcell currents. The sum of the modelled absorption inside the three junctions is shown in white. The data points are the sum of the measured external quantum efficiency. (B) Power loss due to parasitic absorption in different parts of the triple-junction solar cell. The given percentage numbers are the fraction of the total optical loss. [Colour figure can be viewed at wileyonlinelibrary.com]

layer absorb only an insignificant amount of light. The shading by the metal finger grid on the front side of the solar cell was calculated by geometrical considerations of the finger width and spacing. It agrees with the optical modelling but could not be deduced reliably from the measured data directly due to the smallness of its value. Note that the coloured areas in Figure 7A refer to number of photons, irrespective of their energy, while the contributions in Figure 7B are weighted by energy. Hence, they appear different in size.

Without changes to the structure, the absorber thicknesses and band gaps of the presented device could be optimised for achieving current match at 12.9 mA/cm². As discussed above this would result in a current density gain of 0.3 mA/cm² translating to an efficiency of 36.5% under AM1.5g. This is the first step of the roadmap towards further improvements. The next step could be the insertion of a four-layer instead of a two-layer ARC which would decrease reflection losses in the usable wavelength range by around 0.3 mA/cm² corresponding to a short-circuit current density gain of 0.1 mA/cm². Yet a material combination that does not lead to increased parasitic absorption in the ARC layers must be found. The commonly used MgF_2/ $ZnS/MgF_2/ZnS$ Herpin-ARC for instance has higher parasitic absorption compared to a two-layer ARC of MgF_2/Ta_2O_5. If the thickness of the AlInP window layer could be decreased by 10 nm without loss in its function as front-surface field, the current loss could be reduced from 0.60 to 0.22 mA/cm². Another 0.4 mA/cm² could be gained by using more transparent and thinner tunnel-junction layers such as AlGaInP or AlGaAs instead of GaInP and GaAs in the upper tunnel diode. From the bond layer, there is only a small current potential of up to 0.1 mA/cm² to be expected if a GaInP/Si direct wafer bond can be established. Hence, taken everything together, from an optical perspective in a practical limit a j_{sc} of 13.3 mA/cm² and an efficiency of 37.6% under AM1.5g could be obtained.

The difference between the modelled absorption, shown by the white area in Figure 7, and the measured external quantum efficiency indicates the amount of electrical loss inside the subcells. While the top cell is entirely absorption limited, a discrepancy between absorption and quantum efficiency in the middle and bottom cell implies the occurrence of transport losses. For the middle cell, this could be related to a smaller hole mobility in the n-GaInAsP absorber resulting in a reduced diffusion length despite a higher hole lifetime compared to p-GaInAsP. For single rear-heterojunction GaInAsP solar cells with such an absorber thickness, no diffusion length limitation was observable.[12] Thus, it seems the incorporation into the triple-junction between two tunnel diodes and the higher thermal load during the top cell overgrowth had a detrimental effect on the diffusion length. As for the bottom cell, the main loss mechanism is recombination at the cell perimeter. Because of the long diffusion lengths in the indirect semiconductor silicon, many generated charge carriers reach the unpassivated mesa trenches and recombine at the surface. In a previous publication, we have shown that the efficiency loss associated with perimeter recombination amounts to 1%$_{abs}$, caused both by a voltage decrease and by a current decrease.[14] For the 4 cm² solar cells of this study, edge recombination in the silicon bottom cell is a significantly more severe issue than in industrial-size solar cells of 243 cm².

4 | CONCLUSIONS

We presented a III-V//Si triple-junction solar cell with a GaInP top cell, a GaInAsP middle cell, and a silicon bottom cell exhibiting a conversion efficiency of 36.1%, the highest efficiency reported for a Si-based multi-junction solar cell reported to date. The III-V top cell structure was wafer-bonded to the silicon bottom cell for a monolithic

integration. A metallodielectric back-side reflector was integrated to optimise light trapping in the Si bottom cell. By employing a rear-heterojunction cell design in both the middle and top cell, the open-circuit voltage of the triple-junction device could be improved by 61 mV compared to previous generations. Due to the high minority carrier lifetime of the n-absorber material, the external radiative efficiency is higher compared to a reference device with a homojunction cell design. Since radiative recombination of minority carriers is dominant in this structure, strong luminescent coupling between the middle and bottom subcell was observed. This was carefully considered for accurate quantification of the external quantum efficiency. An absolute determination of the external quantum efficiency of every subcell was important for evaluating the current gain caused by the back-side reflector. Acquiring current–voltage curves at systematically varying irradiance conditions selectively for each subcell is a useful method for obtaining the luminescence coupling factors and the externally injected currents for calibration of the external quantum efficiency.

Remaining losses are mainly due to non-absorption and parasitic absorption inside the diffractive rear-side structure. Photons with a lower energy than 1.12 eV that escape after reflection at the rear side could in principle be recycled by luminescent up-conversion.[31] The main remaining optical loss channel is front-side reflection, as a transfer-matrix analysis of the layer stack has revealed. This could be addressed in the future for instance by a four-layer anti-reflection coating. The electrical losses in the silicon bottom cell due to surface recombination at the unpassivated mesa trenches will be alleviated in the future if this technology is scaled to larger solar cell sizes.

ACKNOWLEDGEMENTS

CONFLICT OF INTEREST STATEMENT

The authors have no conflict of interests to declare.

DATA AVAILABILITY STATEMENT

The data that support the findings of this study are available from the corresponding author upon reasonable request.

ORCID

Patrick Schygulla https://orcid.org/0000-0001-9103-1045
Ralph Müller https://orcid.org/0000-0001-6248-3659
Oliver Höhn https://orcid.org/0000-0002-5991-2878
David Chojniak https://orcid.org/0000-0001-9010-4468
Andrea Cordaro https://orcid.org/0000-0003-3000-7943
Stefan Tabernig https://orcid.org/0000-0002-6471-8527
Benedikt Bläsi https://orcid.org/0000-0003-1624-1530
Albert Polman https://orcid.org/0000-0002-0685-3886
Gerald Siefer https://orcid.org/0000-0001-9387-0010
David Lackner https://orcid.org/0000-0001-8170-0874
Frank Dimroth https://orcid.org/0000-0002-3615-4437

REFERENCES

1. Richter A, Hermle M, Glunz SW. Reassessment of the limiting efficiency for crystalline silicon solar cells. *IEEE J Photovolt*. 2013;3(4): 1184-1191. doi:10.1109/JPHOTOV.2013.2270351
2. Veith-Wolf BA, Schäfer S, Brendel R, Schmidt J. Reassessment of intrinsic lifetime limit in n-type crystalline silicon and implication on maximum solar cell efficiency. *Sol Energy Mater sol Cells*. 2018;186: 194-199. doi:10.1016/j.solmat.2018.06.029
3. Benda V, Černá L. PV cells and modules - state of the art, limits and trends. *Heliyon*. 2020;6(12):e05666. doi:10.1016/j.heliyon.2020. e05666
4. France RM, Geisz JF, Song T, et al. Triple-junction solar cells with 39.5% terrestrial and 34.2% space efficiency enabled by thick quantum well superlattices. *Joule*. 2022;6(5):1121-1135. doi:10.1016/j. joule.2022.04.024
5. Cariou R, Benick J, Feldmann F, et al. III−V-on-silicon solar cells reaching 33% photoconversion efficiency in two-terminal configuration. *Nat Energy*. 2018;3(4):326-333. doi:10.1038/s41560-018-0125-0
6. Lackner D, Höhn O, Müller R, et al. Two-terminal direct wafer-bonded GaInP/AlGaAs//Si triple-junction solar cell with AM1.5g efficiency of 34.1%. *Sol RRL*. 2020;4(9). doi:10.1002/solr.202000210
7. Schygulla P, Müller R, Lackner D, et al. Two-terminal III−V//Si triple-junction solar cell with power conversion efficiency of 35.9% at AM1.5g. *Prog Photovolt Res Appl*. 2022;30(8):869-879. doi:10.1002/ pip.3503
8. Essig S, Allebé C, Remo T, et al. Raising the one-sun conversion efficiency of III−V/Si solar cells to 32.8% for two junctions and 35.9% for three junctions. *Nat Energy*. 2017;2(9):17144. doi:10.1038/nenergy. 2017.144
9. Tockhorn P, Sutter J, Cruz A, et al. Nano-optical designs for high-efficiency monolithic perovskite-silicon tandem solar cells. *Nat Nanotechnol*. 2022;17(11):1214-1221. doi:10.1038/s41565-022-01228-8 https://www.nature.com/articles/s41565-022-01228-8
10. Zheng J, Wang G, Duan W, et al. Monolithic perovskite–perovskite–silicon triple-junction tandem solar cell with an efficiency of over 20%. *ACS Energy Lett*. 2022;7(9):3003-3005. doi:10.1021/ acsenergylett.2c01556
11. Makita K, Mizuno H, Tayagaki T, et al. III-V//Si multijunction solar cells with 30% efficiency using smart stack technology with Pd nanoparticle array. *Prog Photovolt Res Appl*. 2019;42(8):16-24. doi:10. 1002/pip.3200
12. Schygulla P, Heinz FD, Dimroth F, Lackner D. Middle cell development for wafer-bonded III-V//Si tandem solar cells. *IEEE J Photovolt*. 2021;11(5):1264-1270. doi:10.1109/JPHOTOV.2021.3090159
13. Hwang S-T, Kim S, Cheun H, et al. Bandgap grading and Al0.3Ga0.7As heterojunction emitter for highly efficient GaAs-based solar cells. *Sol Energy Mater sol Cells*. 2016;155:264-272. http://www.sciencedirect. com/science/article/pii/S0927024816301817. doi:10.1016/j.solmat. 2016.06.009

14. Müller R, Schygulla P, Lackner D, et al. Silicon-based monolithic triple-junction solar cells with conversion efficiency >34%. In 37th European Photovoltaic Solar Energy Conference and Exhibition, Lisbon, Portugal. 2020:574–578.

15. Kirchartz T, Rau U, Hermle M, Bett AW, Helbig A, Werner JH. Internal voltages in GaInP/GaInAs/Ge multijunction solar cells determined by electroluminescence measurements. *Appl Phys Lett*. 2008;92(12):123502-123503. doi:10.1063/1.2903101

16. Scherff MLD, Nutter J, Fuss-Kailuweit P, Suthues J, Brammer T. Spectral mismatch and solar simulator quality factor in advanced LED solar simulators. *Jpn J Appl Phys*. 2017;56(8S2):08MB24. doi:10.7567/JJAP.56.08MB24

17. Chojniak D, Bett AJ, Hohl-Ebinger J, Reichmuth SK, Schachtner M, Siefer G. LED solar simulators – a spectral adjustment procedure for tandem solar cells. *AIP Conf Proc*. 2023;2826(1):30003, https://pubs.aip.org/aip/acp/article/2826/1/030003/2900409

18. Bläsi B, Höhn O, Hauser H, et al. Photonic structures for III-V//Si multijunction solar cells with efficiency >33%. In: *Photonics for Solar Energy Systems VII*. Strasbourg; 2018:2.

19. McMahon WE, Emery KE, Friedman DJ, et al. Fill factor as a probe of current-matching for GaInP 2/GaAs tandem cells in a concentrator system during outdoor operation. *Prog Photovolt Res Appl*. 2008;16(3):213-224. doi:10.1002/pip.798

20. Sinton RA. Possibilities for process-control monitoring of electronic material properties during solar-cell manufacture. In Proceedings 9th Workshop on Crystalline Silicon Solar Cell Materials and Processes. 67–73.

21. Suckow S, Pletzer TM, Kurz H. Fast and reliable calculation of the two-diode model without simplifications. *Prog Photovolt Res Appl*. 2014;22(4):494-501. doi:10.1002/pip.2301

22. Steiner M, Geisz JF. Non-linear luminescent coupling in series-connected multijunction solar cells. *Appl Phys Lett*. 2012;100(25):251106. doi:10.1063/1.4729827

23. Ragay FW, Ruigrok E, Wolter JH. GaAs-AlGaAs heterojunction solar cells with increased open-circuit voltage. In: *24th IEEE Photovoltaic Specialists Conference (PVSC): IEEE 1st World Conference on Photovoltaic Energy Conversion*. Waikoloa, HI, USA; 1994:1934-1937.

24. Green MA, Ho-Baillie AWY. Pushing to the limit: radiative efficiencies of recent mainstream and emerging solar cells. *ACS Energy Lett*. 2019;4(7):1639-1644. doi:10.1021/acsenergylett.9b01128

25. Steiner M, Geisz JF, Moriarty TE, et al. Measuring IV curves and subcell photocurrents in the presence of luminescent coupling. *IEEE J Photovolt*. 2013;3(2):879-887. doi:10.1109/JPHOTOV.2012.2228298

26. Aspnes DE, Studna AA. Dielectric functions and optical parameters of Si, Ge, GaP, GaAs, GaSb, InP, InAs, and InSb from 1.5 to 6.0 eV. *Phys Rev B, Condens Matter Mater Phys*. 1983;27(2):985-1009. doi:10.1103/PhysRevB.27.985

27. Pierce DT, Spicer WE. Electronic structure of amorphous Si from photoemission and optical studies. *Phys Rev B, Solid State*. 1972;5(8):3017-3029. doi:10.1103/PhysRevB.5.3017

28. Harbecke B. Coherent and incoherent reflection and transmission of multilayer structures. *Appl Phys B*. 1986;39(3):165-170, https://link.springer.com/article/10.1007/BF00697414

29. Byrnes SJ. Multilayer optical calculations. 2016//2016. [Online] Available: https://arxiv.org/pdf/1603.02720

30. Schygulla P, Fuß-Kailuweit P, Höhn O, Dimroth F. Determination of the complex refractive index of compound semiconductor alloys for optical device modelling. *J Phys D Appl Phys*. 2020;53(49):495104. doi:10.1088/1361-6463/abb270

31. Trupke T, Shalav A, Richards BS, Würfel P, Green MA. Efficiency enhancement of solar cells by luminescent up-conversion of sunlight. *Sol Energy Mater sol Cells*. 2006;90(18–19):3327-3338. doi:10.1016/j.solmat.2005.09.021